Supplementary Materials for

"Unraveling a midcrustal seismogenic fault structure from a seismic sequence and geophysical data: application to the 28 October 2022 M_L4.1 Goesan earthquake in the central Korean Peninsula"

Tae-Kyung Hong[1*], Junhyung Lee[1], Jeongin Lee[1], Seongjun Park[1], Byeongwoo Kim[1], and Sungchan Choi[2]

Affiliation and address:

[1]Yonsei University, Department of Earth System Sciences, 50 Yonsei-ro, Seodaemun-gu Seoul 03722, South Korea.

[2]Geo-information Institute, GI Co. Ltd., Busan 47598, South Korea.

Correspondence to:

tkhong@yonsei.ac.kr (Tae-Kyung Hong)

Contents of this file

Introduction

This supplementary materials provide additional materials with figures.

Data points for (a) average shear-wave velocity within the top 30 m from the surface (V_{S30}), (b) Bouguer gravity anomalies, (c) magnetic anomalies, and (d) surface heat flux of the study region. The mainshock location (circle) and lineaments (solid lines) are indicated.

Additional information

The 28 October 2022 M_L4.1 earthquake produced strong ground motions in local and regional distances (Fig. S1). The peak ground accelerations and peak ground velocities induced by the earthquake are large in local distances (Fig. S2). The data points of average shear-wave velocity within the top 30 m from the surface (V_{S30}), Bouguer gravity anomalies, magnetic anomalies, and surface heat flux are presented (Fig. S3). The numbers of data points and spatial coverages vary by the data type. The data points are interpolated over the study region.

The mainshock incurred a series of aftershocks. A matched filter analysis enables us to detect micro events in the source region (Fig. S4). The detected micro events vary depending on the threshold level in waveform correlations. The detected micro events are distributed around the mainshock and reported events (Fig. S5). The foreshocks, mainshock and aftershocks reported by a local agency (Korea Meteorological Administration) are relocated using a conventional hypocentral inversion method (VELHYPO). VELHYPO is a joint inversion method that yields hypocentral parameters and optimum velocity models. The inverted velocity models are close to a local average 1-D velocity model for the Korean Peninsula (Fig. S6). The similar inverted velocity structures suggest that the average 1-D velocity models of the Korean Peninsula may be applicable for the region.

The seismic waveforms of the relocated events are presented (Figs. S7-S16). The events

are well recorded in dozens of stations in local distances. The P and S phases of waveform records fit well with the traveltime curves.

References

Chang, S.-J. and Baag, C.-E. (2006). Crustal structure in southern Korea from joint analysis of regional broadband waveforms and travel times. Bulletin of the Seismological Society of America, 96, 856-870.

Kennett, B. L. N., Engdahl, E. R., and Buland, R. (1995). Constraints on seismic velocities in the Earth from traveltimes. Geophysical Journal International, 122, 108-124.

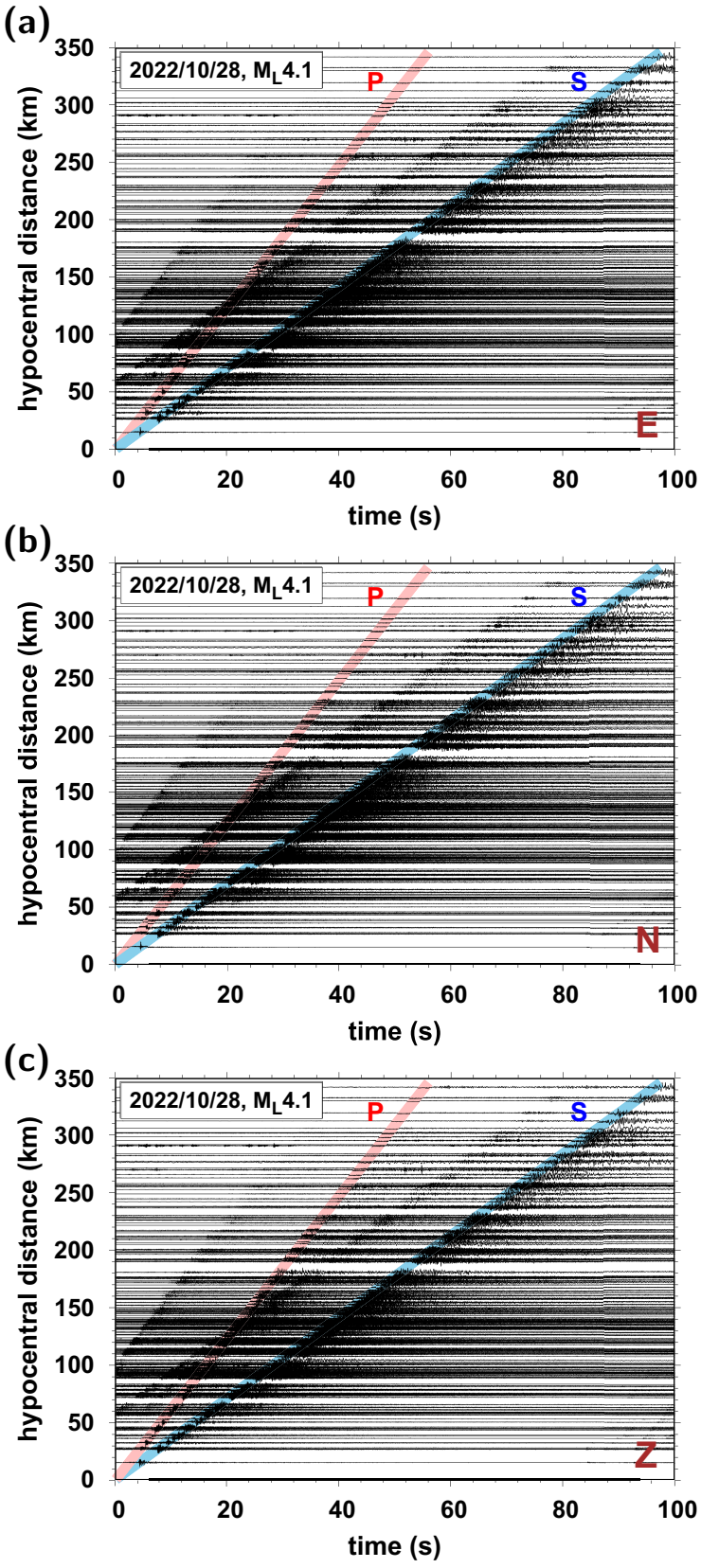

Figure S1. Seismic waveform records of the mainshock in (a) EW, (b) NS, and (c) vertical components. The P and S phases are marked.

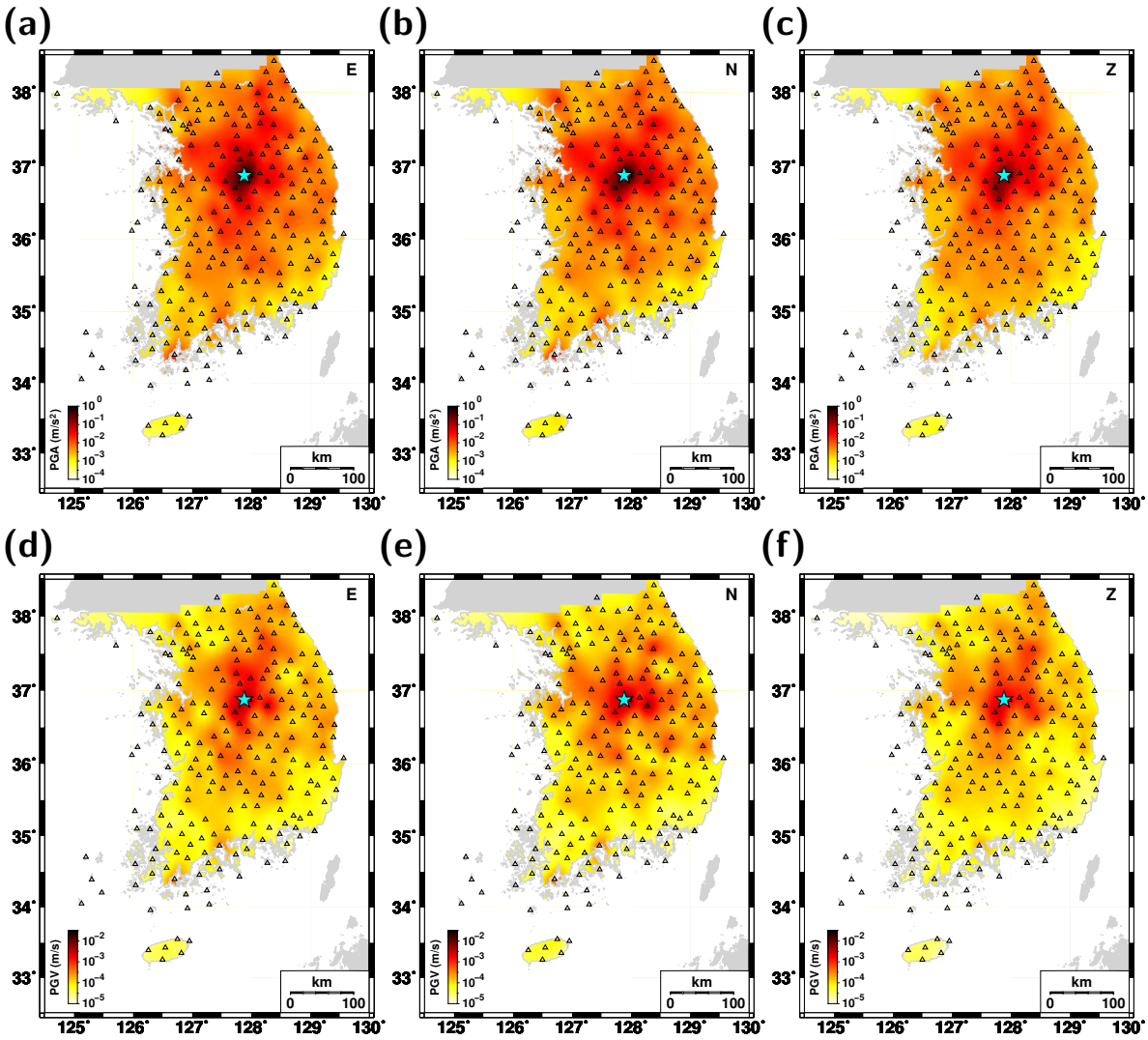

Figure S2. Mainshock inducing peak ground accelerations (PGAs) in (a) EW, (b) NS, and (c) vertical components, and peak ground velocities (PGVs) in (d) EW, (e) NS, and (f) vertical components. The stations (triangles) and event epicenter (star) are marked.

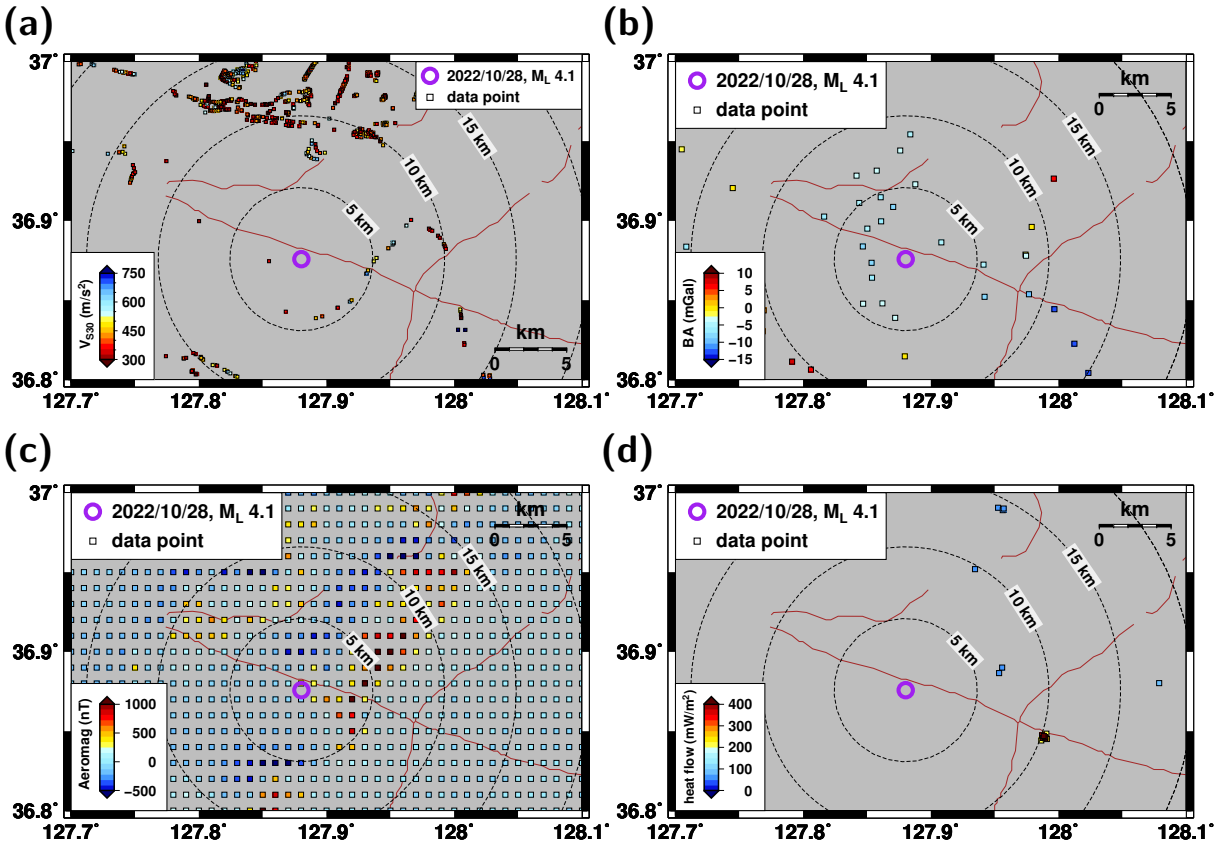

Figure S3. Data points for (a) average shear-wave velocity within the top 30 m from the surface (V_{S30}), (b) Bouguer gravity anomalies, (c) magnetic anomalies, and (d) surface heat flux of the study region. The mainshock location (circle) and lineaments (solid lines) are indicated.

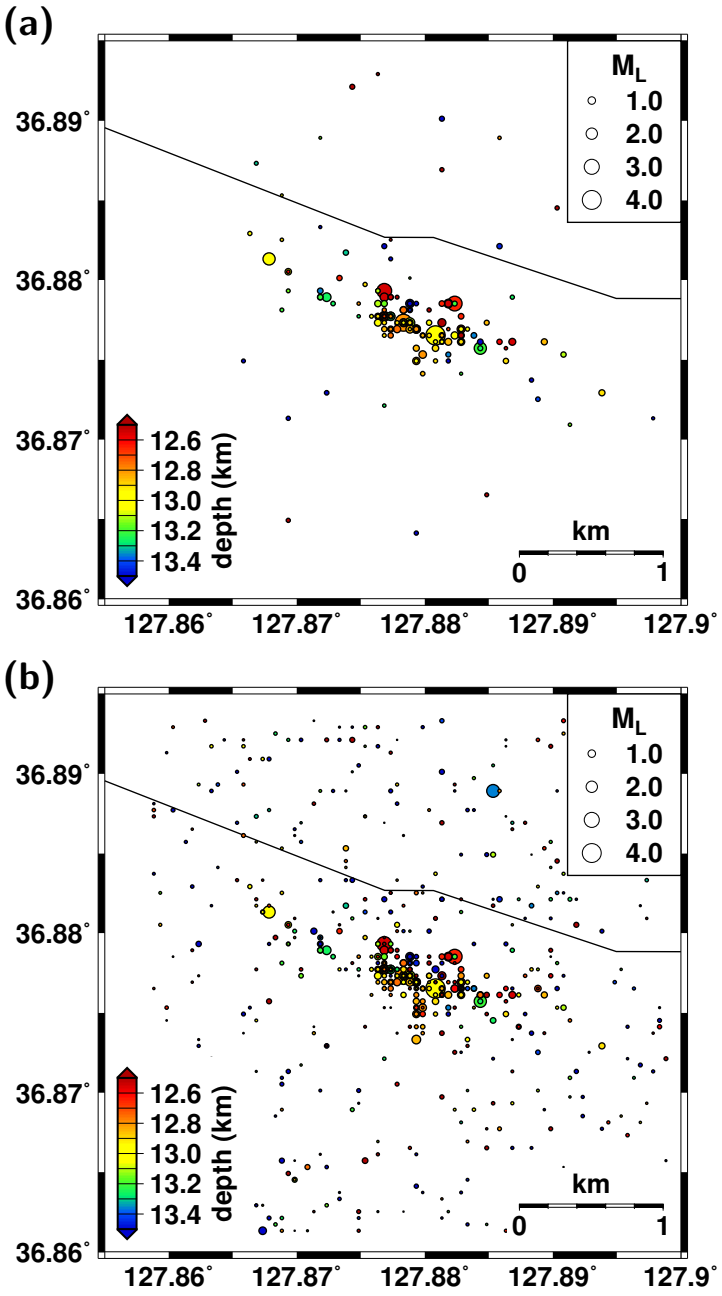

Figure S4. Earthquakes searched by a matched filter analysis: event declaration with correlation coefficients greater than (a) 20 and (b) 10 times the median correlation coefficient for the background noise. The detected events with large correlation coefficients are located around the event cluster.

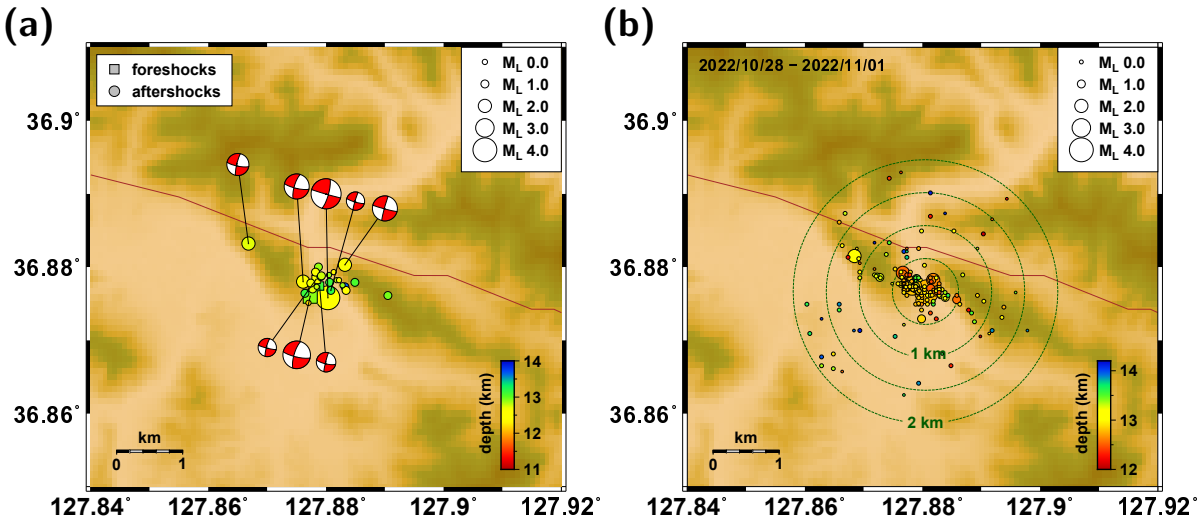

Figure S5. (a) Distribution of reported earthquakes with focal mechanism solutions and (b) micro events detected by the matched filter analysis. The equidistance contours are presented around the mainshock. The detected events are distributed in distances less than 2 km.

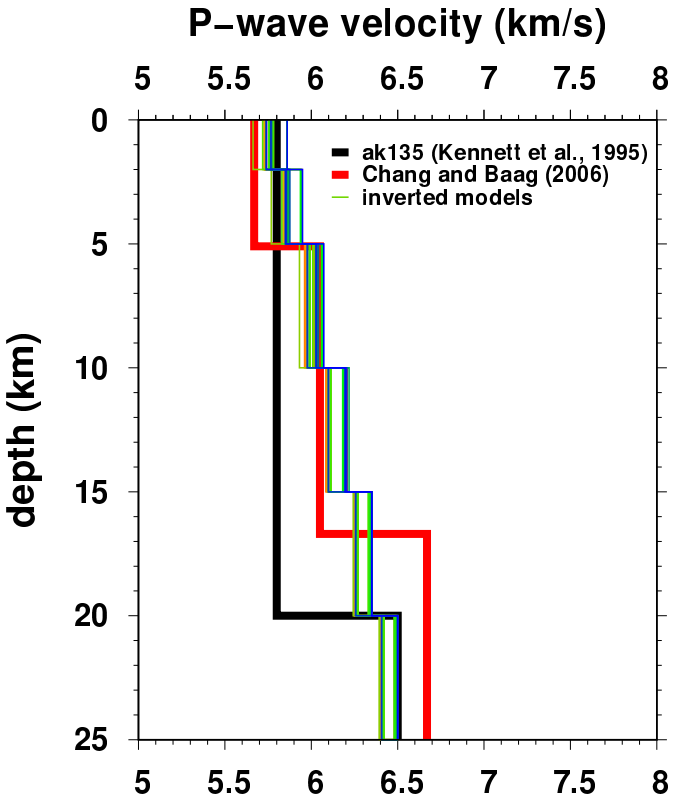

Figure S6. Inverted P velocity models from VELHYPO. The inverted velocity models are compared with a global average 1-D velocity model (ak135) (Kennett et al., 1995) and local average 1-D velocity model (Chang and Baag, 2006). The inverted velocity models are close to the local 1-D velocity model.

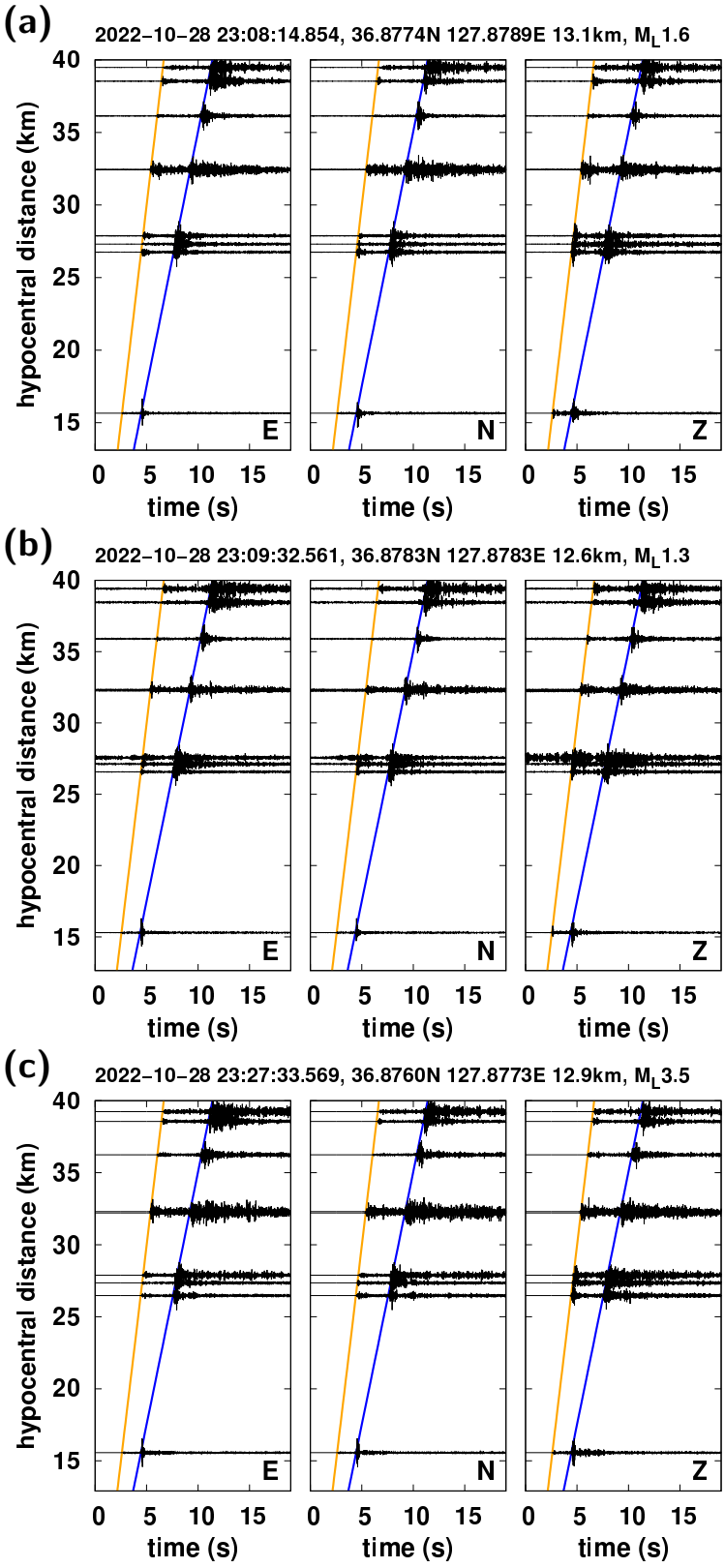

Figure S7. Three-component seismic waveform records of (a) the 28 October 2022 M_L1.6 earthquake, (b) the 28 October 2022 M_L1.3 earthquake and (c) the 28 October 2022 M_L3.5 earthquake. The traveltime curves of P and S phases are marked. The focal depths are presented.

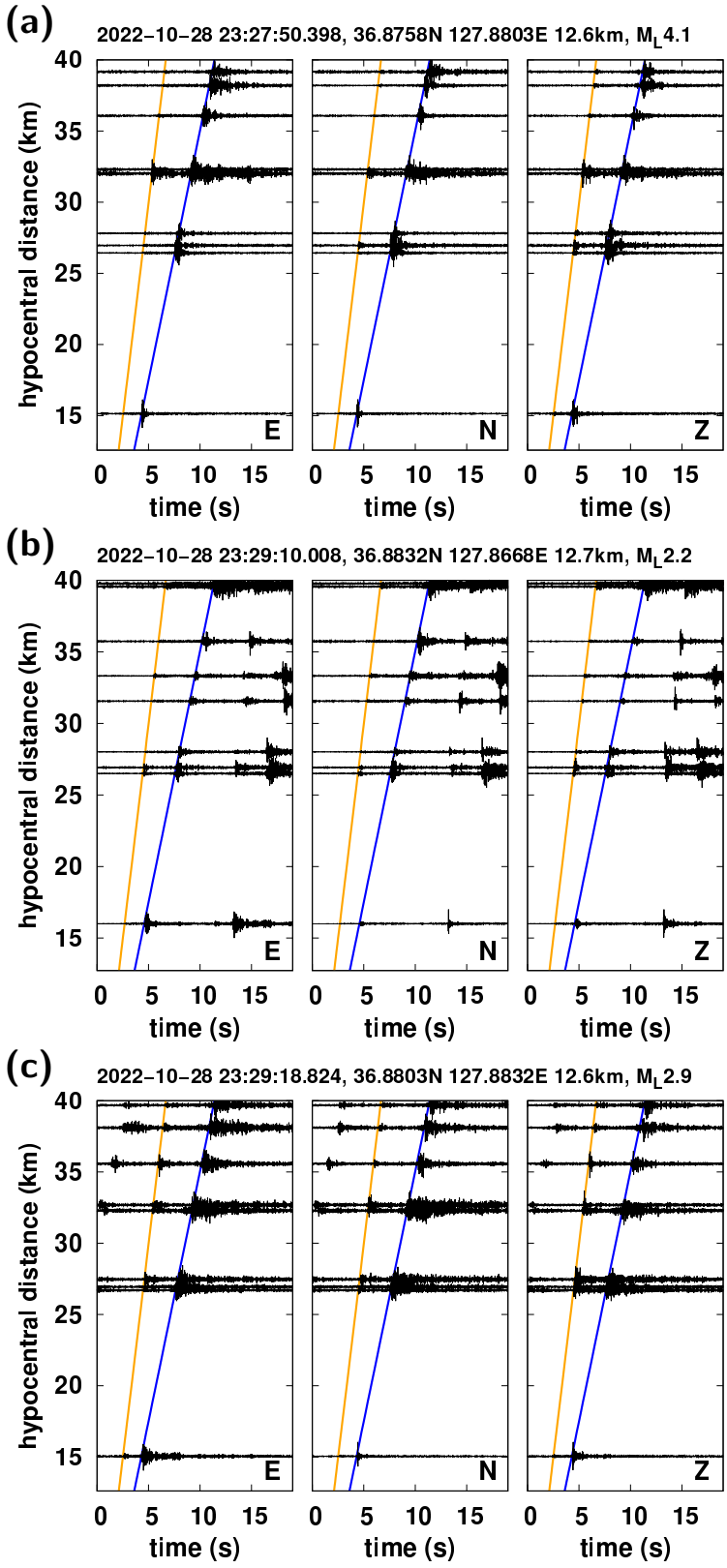

Figure S8. Three-component seismic waveform records of (a) the 28 October 2022 M_L4.1 earthquake, (b) the 28 October 2022 M_L2.2 earthquake and (c) the 28 October 2022 M_L2.9 earthquake. The traveltime curves of P and S phases are marked. The focal depths are presented.

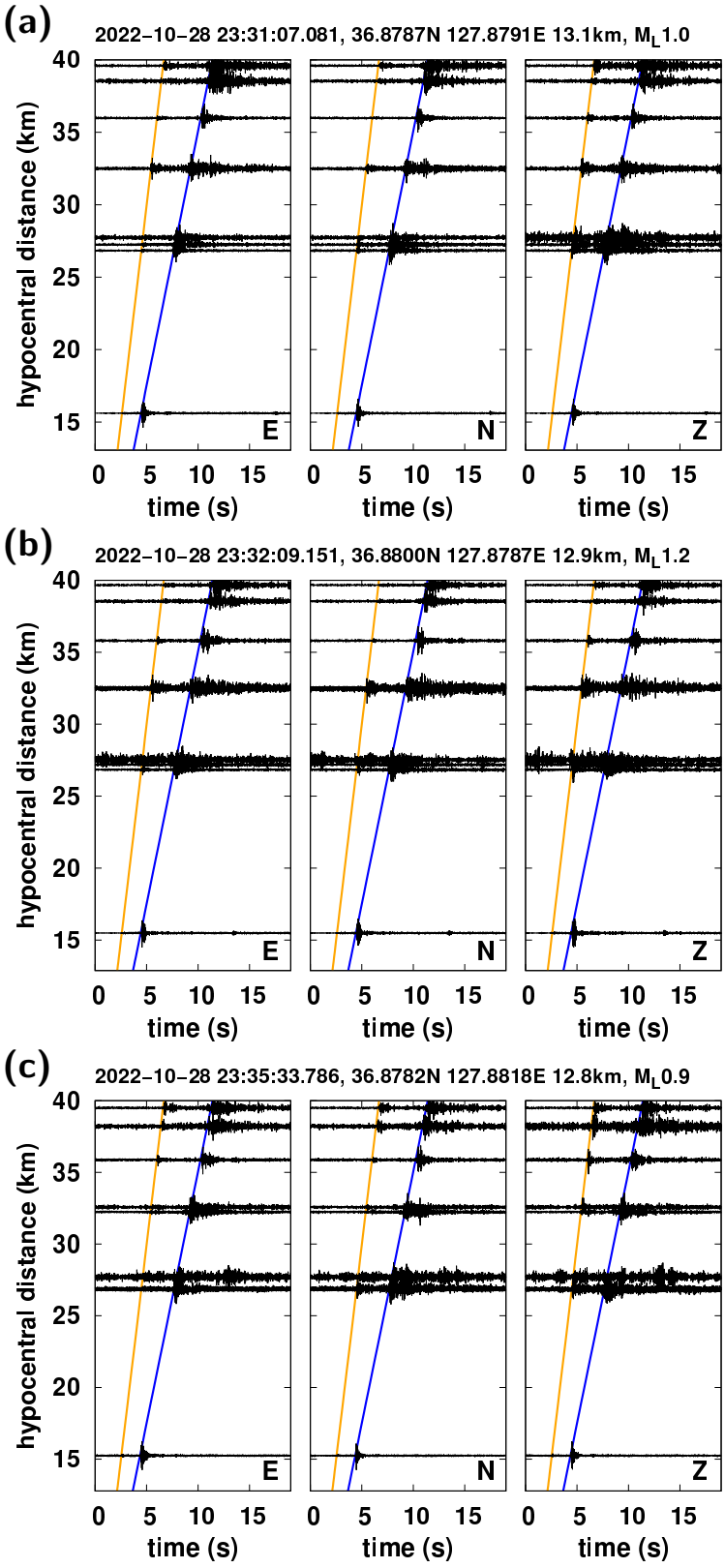

Figure S9. Three-component seismic waveform records of (a) the 28 October 2022 M_L1.0 earthquake, (b) the 28 October 2022 M_L1.2 earthquake and (c) the 28 October 2022 M_L0.9 earthquake. The traveltime curves of P and S phases are marked. The focal depths are presented.

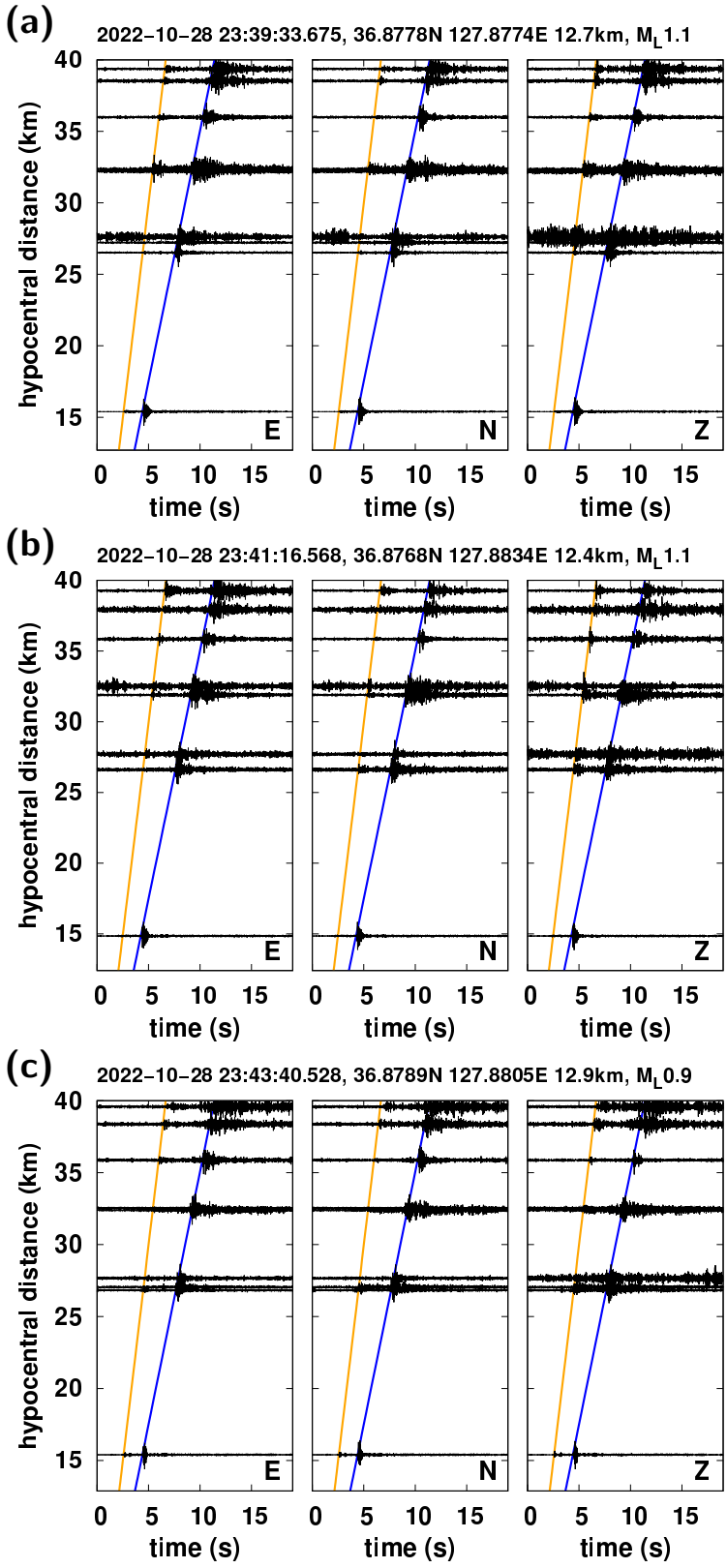

Figure S10. Three-component seismic waveform records of (a) the 28 October 2022 M_L1.1 earthquake with focal depth 12.7 km, (b) the 28 October 2022 M_L1.1 earthquake with focal depth 12.4 km and (c) the 28 October 2022 M_L0.9 earthquake with focal depth 12.9 km. The traveltime curves of P and S phases are marked.

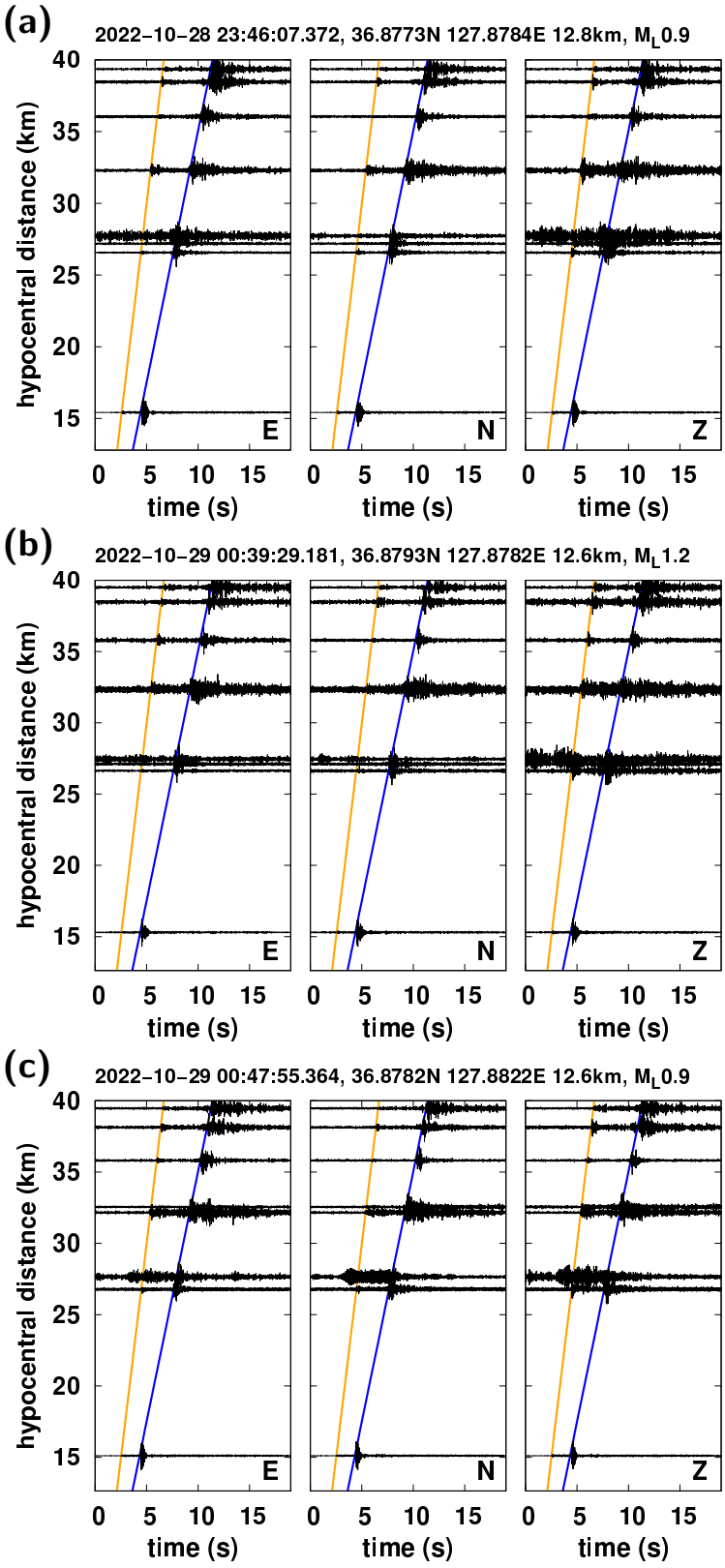

Figure S11. Three-component seismic waveform records of (a) the 28 October 2022 M_L0.9 earthquake with focal depth 12.8 km, (b) the 29 October 2022 M_L1.2 earthquake with focal depth 12.6 km and (c) the 29 October 2022 M_L0.9 earthquake with focal depth 12.6 km. The traveltime curves of P and S phases are marked.

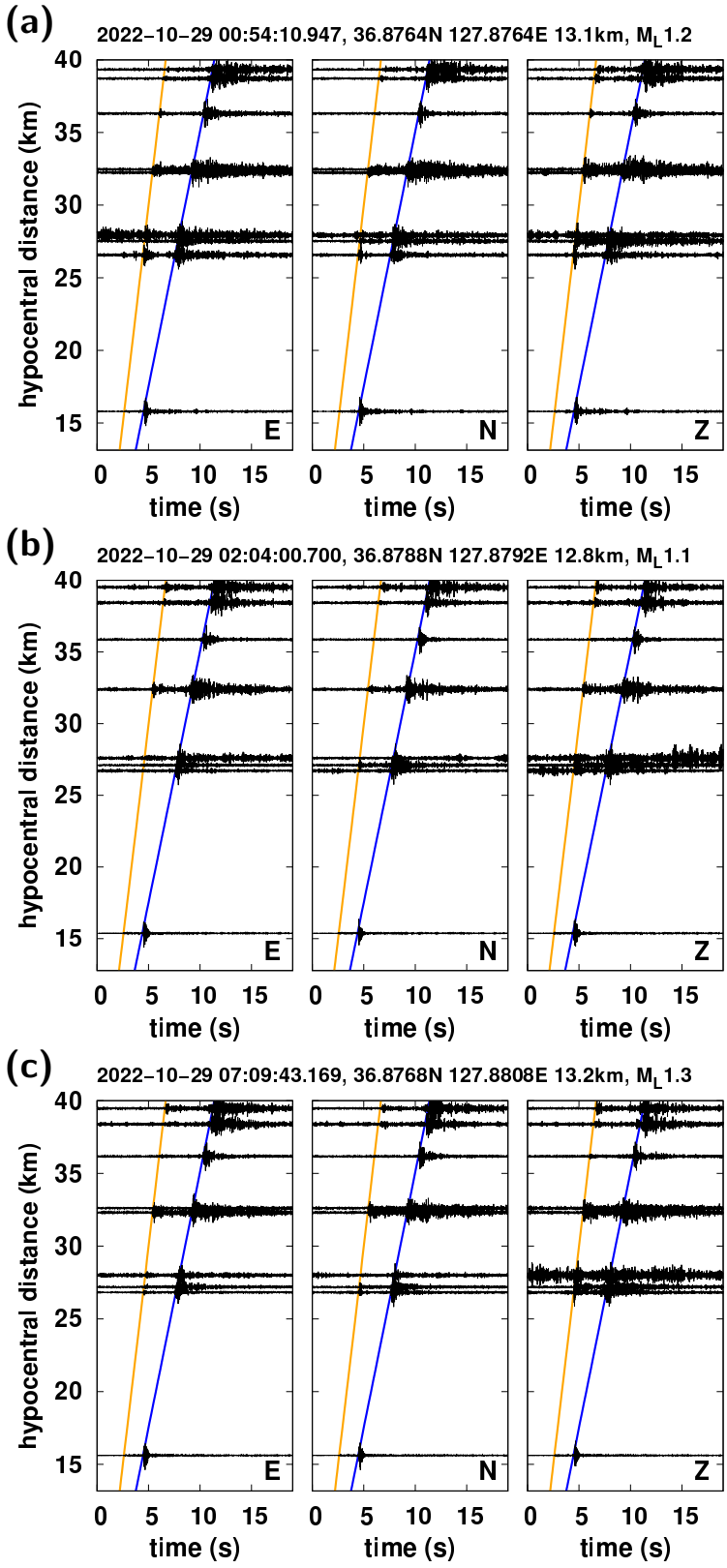

Figure S12. Three-component seismic waveform records of (a) the 29 October 2022 M_L1.2 earthquake with focal depth 13.1 km, (b) the 29 October 2022 M_L1.1 earthquake with focal depth 12.8 km and (c) the 29 October 2022 M_L1.3 earthquake with focal depth 13.2 km. The traveltime curves of P and S phases are marked.

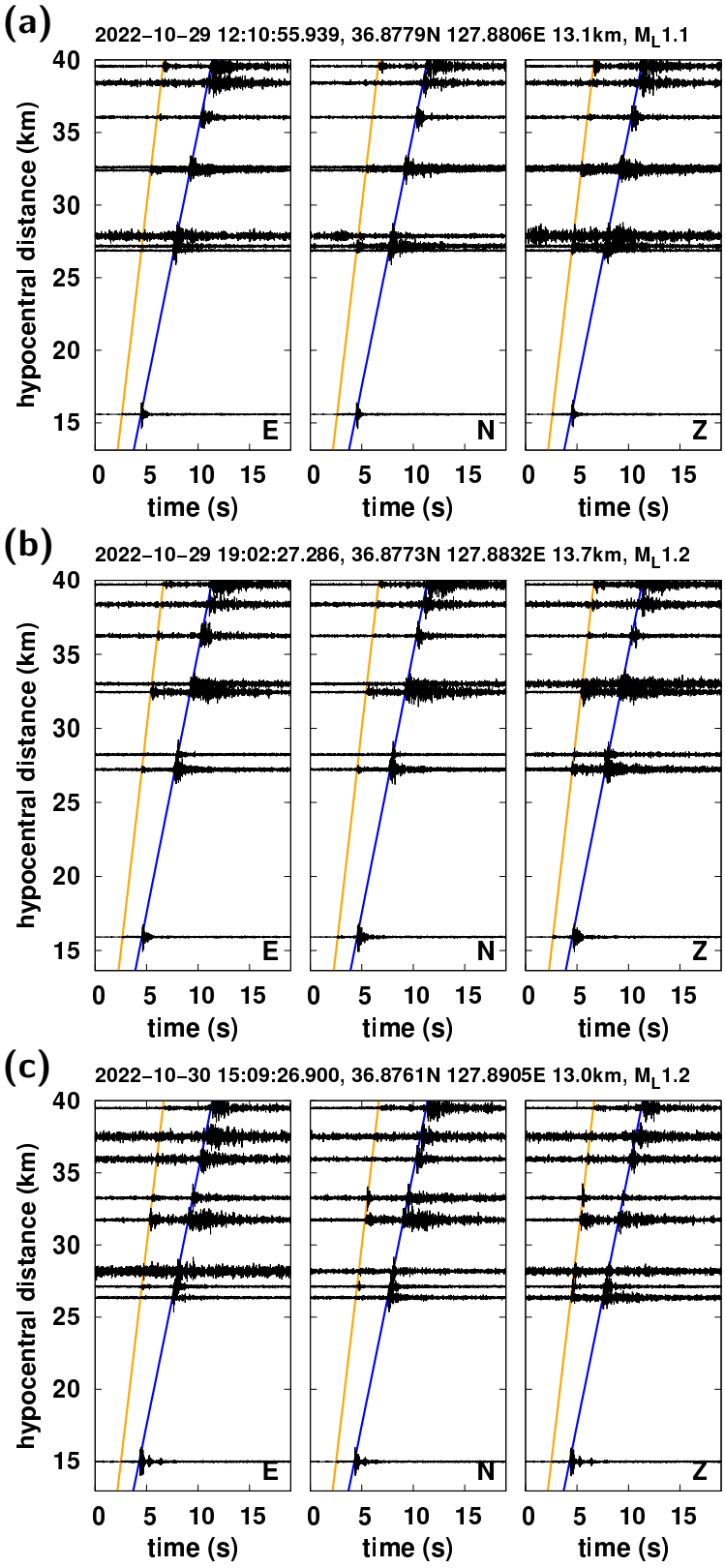

Figure S13. Three-component seismic waveform records of (a) the 29 October 2022 M_L1.1 earthquake with focal depth 13.1 km, (b) the 29 October 2022 M_L1.2 earthquake with focal depth 13.7 km and (c) the 29 October 2022 M_L1.2 earthquake with focal depth 13.0 km. The traveltime curves of P and S phases are marked.

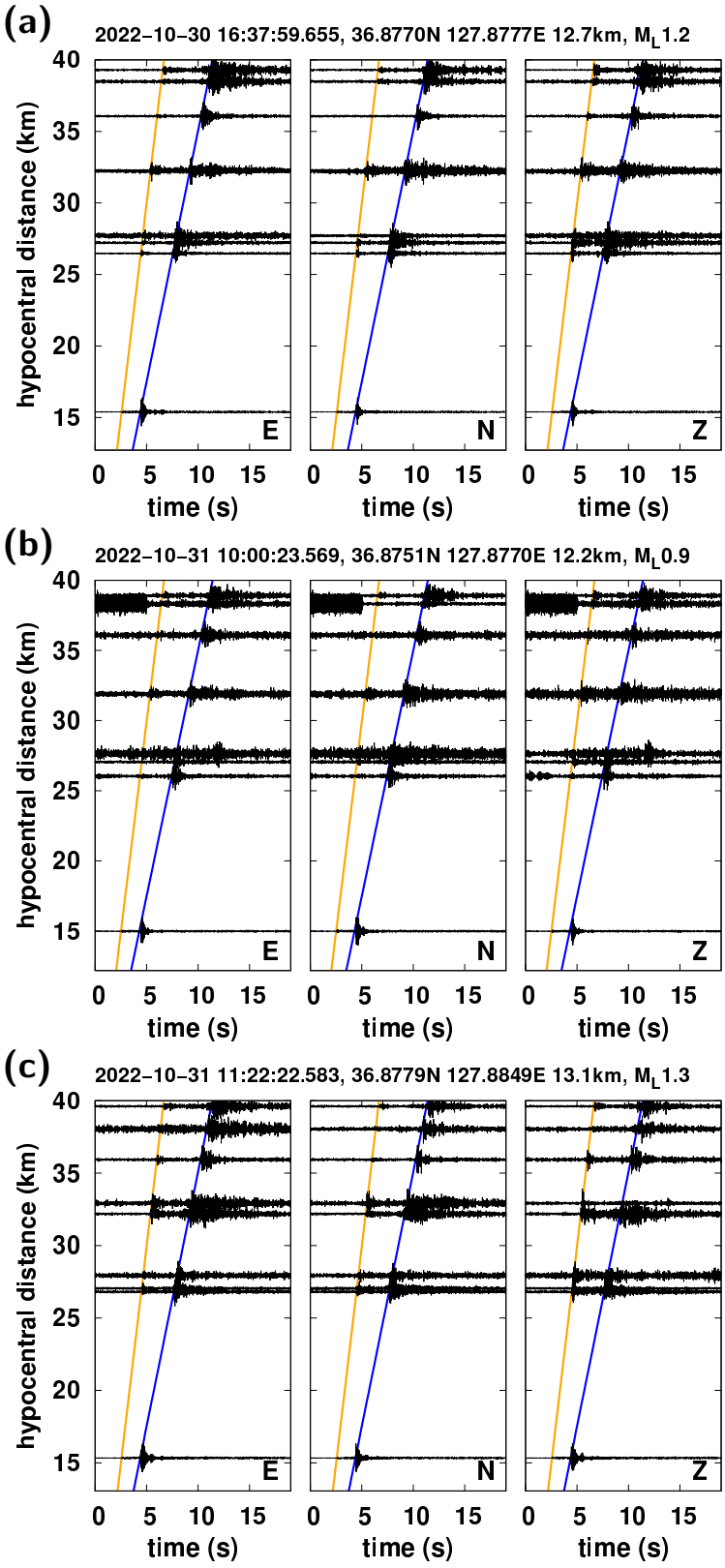

Figure S14. Three-component seismic waveform records of (a) the 30 October 2022 M_L1.2 earthquake with focal depth 12.7 km, (b) the 31 October 2022 M_L0.9 earthquake with focal depth 12.2 km and (c) the 31 October 2022 M_L1.3 earthquake with focal depth 13.1 km. The traveltime curves of P and S phases are marked.

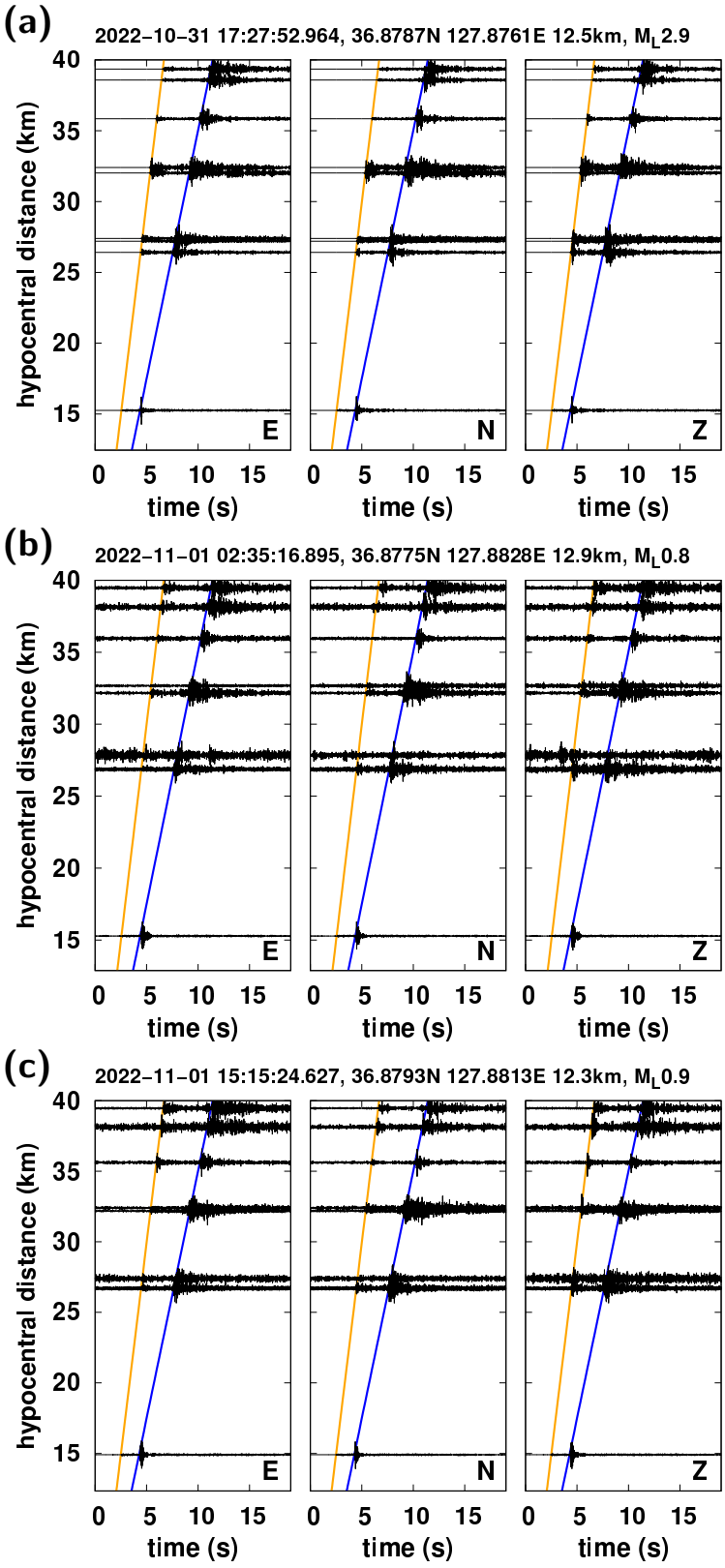

Figure S15. Three-component seismic waveform records of (a) the 31 October 2022 M_L2.9 earthquake with focal depth 12.5 km, (b) the 1 November 2022 M_L0.8 earthquake with focal depth 12.9 km and (c) the 1 November 2022 M_L0.9 earthquake with focal depth 12.3 km. The traveltime curves of P and S phases are marked.

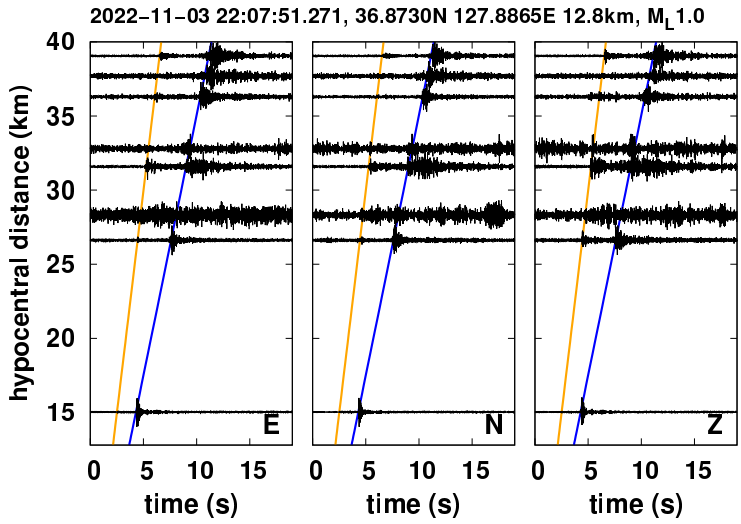

Figure S16. Three-component seismic waveform records of the 3 November 2022 M_L1.0 earthquake with focal depth 12.8 km. The traveltime curves of P and S phases are marked.